Gómez-Villalba, L.S., Sierra-Fernández, A., Milosevic, O., Fort, R., Rabanal, M.E. (2017). Atomic scale study of the dehydration/structural transformation in micro and nanostructured brucite (Mg(OH)2) particles: Influence of the hydrothermal synthesis conditions. *Advanced Powder Technology*, vol. 28, n. 1, pp. 61-72.
DOI: https://doi.org/10.1016/j.apt.2016.08.014

Atomic scale study of the dehydration/structural transformation in micro and nanostructured brucite ($Mg(OH)_2$) particles: Influence of the hydrothermal synthesis conditions

L.S. Gomez-Villalba [a,*], A. Sierra-Fernandez [a,b], O. Milosevic [c], R. Fort [a], M.E. Rabanal [b,d]

[a] Instituto de Geociencias (CSIC, UCM), Calle José Antonio Novais 12, 28040 Madrid, Spain
[b] Carlos III University of Madrid, Materials Science and Engineering and Chemical Engineering Department, Avda. Universidad 30, 28911 Leganés, Madrid, Spain
[c] Institute of Technical Sciences of the Serbian Academy of Sciences and Arts, Knez Mihailova 35/IV, 11000 Belgrade, Serbia
[d] Instituto Tecnológico de Química y Materiales "Álvaro Alonso Barba" (IAAB), Avda. Universidad 30, 28911 Leganés, Madrid, Spain

Keywords:
Brucite
Periclase
Hydrothermal synthesis
TEM-HRTEM-XRD

A B S T R A C T

Micro and nanostructured brucite ($Mg(OH_2)$) particles synthesized by hydrothermal method from solutions with high content of hydrazine (0.14 M) and nitrate (0.24 g) were compared with samples obtained from low hydrazine content (0.0002 M) and nitrate (0.12 g). The samples were heated at 180 °C for 4 h, 6 h and 12 h. XRD, TEM HRTEM, SAED and image analysis techniques were used for the morphological and structural characterization. The effect of electron beam irradiation on the brucite dehydration was observed in atomic resolution images at 300 kV. Hexagonal crystals show differences in crystallinity, strains and kinetic of reaction. High hydrazine/nitrate samples have slightly larger crystals with better crystallinity, showing a strong preferential orientation. Rietveld refinements show how unit cell parameters are bigger in samples obtained with higher hydrazine/nitrate content, confirming also the preferential orientation along the 0001 plane. Differences in the dehydration process show the rapid formation of a porous surface, the amorphised cortex or the presence of highly oriented strains in samples prepared from higher hydrazine/nitrate content. Conversely, crystals slightly smaller with randomly scattered defect surfaces showing the $Mg(OH)_2$/MgO interphase in samples prepared with low hydrazine/nitrate content. Significant differences in the kinetic of reaction indicate how the dehydration process is faster in samples prepared with high hydrazine/nitrate content.

1. Introduction

Brucite ($Mg(OH)_2$) is a mineral widely known due to its multiple applications. Its refractory character [1], and fire retardant properties [2] making it an interesting material for use in the field of energy saving and thermal insulation [3]. Also, magnesium hydroxide is a promising material for chemical heat storage in nuclear reactors [4,5] or in steel coatings [6]. But certainly one of the main applications is to be the precursor of MgO, a material with large properties as catalyst [7]. Even more, the biomedical [8] and pharmaceutical [9] fields have taken advantage of their properties.

Brucite is a representative of the group of hydroxides with compact hexagonal packing (CdI_2 structure, $P\bar{3}m1$). The structure of $Mg(OH)_2$ stratified layers favors the incorporation of different ions modifying its final properties. Among them, the addition of CO_2, from the atmosphere promotes natural carbonation reaction. This important quality has taken advantage to be used as consolidant in conservation of architecture or archaeology for building restoration of the cultural heritage [10]. Besides, its uses include also the restoration of canvas and paints in the field of fine arts [11], or the deacidification of paper [12].

In thermal dehydration, a simple brucite crystal ($Mg(OH)_2$) is converted into a NaCl type MgO cubic crystal ($Fm\bar{3}m$) [13] known as periclase, as the result of a topotactic transformation [14,15]. $Mg(OH)_2$ could also be dehydrated by radiating with high energy electrons [16]. To date, brucite periclase transformation has been studied with transmission electron microscopy by combining imaging and electron diffraction. The understanding of several processes during the *in situ* observation in a TEM has shed light on different research topics. For instance the mechanisms of sintering at

nanometric scale [17] or the formation of MgO by $Mg(OH)_2$ dehydration in a short time [18].

A number of synthesis procedures are in place to obtain nanostructured $Mg(OH)_2$ and MgO, such as sol gel [19], ionic exchange [20], wet precipitation [21,22], solvothermal/hydrothermal techniques [23] or thermal evaporation [24]. Among them, the hydrothermal method is considered a rapid, easy and effective method to control the particle size or morphology. In presence of different surfactants or combined with a calcination process is a useful tool for the synthesis of low dimensional nanomaterials due to its distinct advantages such as its single step process at low temperatures, wide selection of compositions, and morphological control [25]. However, the design of nanoparticles with specific granulometry, shape, chemistry or textural properties, are nowadays the main goal, for getting the most convenient nanoproducts to diverse and advanced applications [26].

Hydrazine, an inorganic compound (N_2H_4) is a highly reactive base, used widely as reducing agent, with low cost, being highly toxic in high and low doses [27,28]. However, to control the structural and surface morphology of nanomaterials, aqueous solutions of hydrazine turn out very useful [29,30]. Besides, the role of nitrates in different concentrations has been demonstrated to be important in the control of particle size [31,32].

In this work, $Mg(OH)_2$ nanoparticles have been synthesized using the hydrothermal method [33], adding hydrate hydrazine as surfactant and nitrate as reagent to the precursor solution. The main goal is to establish differences between two concentrations of hydrazine/nitrate, and to determine their effects on morphology, crystal size, texture, porosity and behavior at atomic level. Besides, the use of electron radiation in a Transmission Electron Microscope allows monitoring the transformation process from brucite to periclase. Previous studies carried out with the same samples [34] demonstrated how the synthesis temperature (150 °C and 180 °C), reaction media and reaction time have a strong influence on the morphology, particle size, agglomeration and crystallographic structures of brucite obtained. Besides, prolonged reaction time improved the crystallinity degree of magnesium hydroxide particles, disposed as defined hexagonal nanoplates in samples obtained at 180 °C and longer reaction time [34].

2. Experimental

2.1. Synthesis

Pure Mg(OH)2 nanoparticles were prepared by hydrothermal method in a conventional autoclave at different reaction times and surfactant concentrations but using the same temperature (180 °C). The common hexa hydrated magnesium nitrate ($Mg(NO_3)_2\,6H_2O$) and hydrazine hydrate, $N_2H_4\,xH_2O$, were used as starting materials. Two different concentrations of hydrazine and nitrates were evaluated. Low concentrations (henceforth LHN) were prepared mixing 0.12 g of magnesium nitrate hexahydrate ($Mg(NO_3)_2 \times 6H_2O$) with 0.08 mL of hydrazine hydrate ($N_2H_4 \times H_2O$, 0.0002 M), and then were dissolved in high purity water (25 mL) under vigorous magnetic stirring at room temperature. Higher concentrations (henceforth HHN) in the reaction media were also prepared by mixing 0.24 g of $Mg(NO_3)_2 \times 6H_2O$ with 2 mL of 0.14 M $N_2H_4 \times H_2O$. In both cases hydrazine hydrate was added dropwise to the magnesium nitrate solution. For the $Mg(OH)_2$ pure phase synthesis, the concentrations of starting materials and the corresponding experimental conditions are given in Table 1.

The mixtures were stirred for 20 min, and placed in a Teflon lined stainless steel autoclave which was sealed and hydrothermally treated in an oven at 180 °C for 4 h, 6 h and 12 h (Table 1). After that, the resulting suspensions were left to cool down to room temperature, and subsequently centrifuged for 15 min at 500 rpm. The precipitates were washed several times with distilled water and ethanol, and dried in an oven at 60 °C with an inert gas atmosphere for 7 h to avoid the $Mg(OH)_2$ carbonation and decomposition reactions.

2.2. Characterization

The structural characterization was carried out by mean of X ray diffraction (XRD), electron diffraction, Analytical Transmission Electron Microscopy (TEM) and High Resolution Transmission Electron Microscopy (HRTEM) techniques.

XRD analyses were recorder in a Philips X'Pert diffractometer with Bragg Brentano geometry operating at 40 kV and 40 mA, employing Cu Kα radiation (λ = 1.54 Å) in the range of 2Θ value between 15° and 90°, a scan step of 0.02° and a time step of 11 s/step. The databases of the Joint Committee of Powder Diffraction Standards version 2015 (JCPDS) and the American Mineralogist Crystal Structure (AMCSD) were used for the phase identification. Unit cell parameters were calculated by Rietveld refinement using the Fullprof program [35]. In all cases, the calculated lattice constants were obtained after 21 parameters of adjustment. TEM was used to study the morphology, particle size and phase transformation process during the dehydration with the electron beam. Samples were taken from ultrasonically dispersed acetone suspensions. A drop of each suspension was placed on a copper grid with a holey carbon film cover. Analytical transmission electron microscopy was carried out in a JEOL JEM 2100 TEM microscope, operating at 200 kV (0.25 nm point to point resolution) equipped with selected area electron diffraction (SAED). HRTEM was used for monitoring the phase transformation during the dehydration process using a JEOL JEM 3000 TEM operating at 300 kV (measurement conditions: lens aperture, 60 μm; condenser aperture, 70 μm; focal beam spot diameter, ~3 nm, 1.7 Å point to point resolution). The interpretation includes the use of Fourier filtered technique for obtaining Fast Fourier transformed (FFT IFFT). Gatan Digital Micrograph software was used to process HRTEM, and SAED patterns.

The porosity study throughout the electron beam irradiation was carried out in very thin edges of the particles avoiding the multi dispersion effects and ensuring reliable images. The interpretation was carried out taking into account the phase contrast effects, which were carefully monitored according to the methodology of Edington [36]. The image J software has been used to calculate the porosity obtained from isolated and very thin particles at low magnification TEM images.

3. Results and discussion

3.1. X ray analysis: effect of experimental conditions

The XRD results carried out in samples with two different experimental conditions applying the same reaction time are displayed in Fig. 1. In Fig. 1a and b, the XRD profiles show a comparison among samples obtained with high hydrazine/nitrate content (HHN) and low hydrazine/nitrate content (LHN) with a short time of reaction (180 °C/4 h, Fig. 1a) and after a prolonged time of reaction (180 °C/12 h, Fig. 1b). In all cases the diffraction peaks are indexed according to the brucite phase ($Mg(OH)_2$, JCPDS = 01 074 2579) showing a strongest peak at 2 theta ~18.6° (0 0 0 1). This peak intensity does not correspond to the typical brucite profile with the strongest peak at 2 theta 37.9° ($10\bar{1}1$), and the second at 18.6° (0 0 0 1). In this case, the inversion in the intensity has been reported in brucite samples subjected to different pressures [37].

Table 1
Experimental conditions used during the hydrothermal synthesis.

$Mg(NO_3)_2{\cdot}6H_2O$ (mmol)	$N_2H_4{\cdot}xH_2O$ (mmol)	Reaction time (h)	Temperature (°C)	$Mg(OH)_2/N_2H_4$ mmolar ratio	Hydrazine hydrate molar ratio (M)	Sample identification
0.468	0.0048	4 6 12	180	9.75	0.24	HHN
0.936	3.6	4 6 12	180	0.25	0.0002	LHN

Owing to the fact that the samples used in this work have been prepared with the hydrothermal method, high pressure and tem perature are used during the reaction [33], so that a strong prefer ential orientation might be feasible to develop.

Besides, differences in the profiles shape are evident among LHN and HHN samples. While samples prepared with low hydra zine/nitrate content, (LHN 180 °C/4 h, bottom profile, Fig. 1a) and (LHN 180 °C/12 h, bottom profile Fig. 1b) show a noisy and broad shape suggesting a short range order due to poor degree of crys tallinity, in the case of HHN samples (Fig. 1a and b, upper profiles), better defined peaks are observed suggesting a higher crystallinity degree.

The Rietveld graphics obtained after the adjustment using the Fullprof program are shown in Fig. 1c f). In this case, the profiles show the refinement of two samples prepared at the same temper ature and time but with different hydrazine/nitrate concentration: HHN 180 °C/6 h (Fig. 1c), LHN 180 °C/6 h (Fig. 1d), HHN 180 °C/12 h (Fig. 1e) and LHN 180 °C/12 h (Fig. 1f). In all cases the experimental profiles are compared to the calculated profiles, where the 0001, 0002 and $10\bar{1}1$ reflections are indexed accord ing to the brucite phase (the calculated Bragg positions are shown in the graphics). However, the profiles corresponding to the differ ence among the observed and calculated intensities show a strong preferential orientation around 18° corresponding to the 0001 reflection in the samples prepared with higher hydrazine/nitrate content (180 °C/6 h and 180 °C/12 h). Therefore it can be deduced that although the heating time be prolonged, the preferential ori entation is still present.

After Rietveld refinements was possible to determine the unit cell parameters obtained for the samples with different concentra tion and time of heating which are plotted in Fig. 1g, for $a = b$ cell parameter and Fig. 1h, for the c cell parameter. As is observed, although in general the cell parameters present similar dimen sions, is possible to determine how the lattice parameters of sam ples prepared with high hydrazine/nitrate content are bigger in comparison to those obtained with samples prepared with low hydrazine/nitrate content. Besides, smaller unit cell parameters are typical of samples with short reaction time (180 °C/4 h). This slight difference indicates how the hydrazine/nitrate content and the time of heating during the synthesis process can even modify the dimensions of unit cell and thereby cause a possible change in the specific properties of the material.

3.2. Effect of experimental conditions on the morphology and particle size

Fig. 2 shows low magnification TEM images of crystals oriented in two directions, as hexagonal platelets and as lamellar shapes, so that many of them correspond to crystals where the c axis is ori ented parallel to electron beam (hexagonal shapes) and others where the c axis is oriented perpendicular (on edge) to electron beam. The hexagonal shape of a brucite crystal is shown in Fig. 2a and is compared with the typical brucite crystal of Fig. 2 (insert) where the $\{0001\}$ and $\{11\bar{2}0\}$ facets are observed. The electron diffraction pattern (Fig. 2d) taken along the $[0001]$ zone axis of brucite allows identify the spots corresponding to this crystallo graphic orientation. According to the experimental conditions used, changes in morphology and particle size are observed, both in samples obtained from high (Fig. 2b, 180/4 h and 2c 180/6 h) and low concentration of hydrazine/nitrate concentrations (Fig. 2e, 180/4 h and Fig. 2f, 180/6 h). The hexagonal flakes oriented mainly along the $\{0001\}$ basal plane, reveal changes in the particle size distribution as denotes the frequency histograms (Fig. 2b′ and c′). In addition, although the typical hexagonal shape is observed, amorphised edges are frequently developed in samples with low concentration of hydrazine/nitrates (Fig. 2e, 180 °C/4 h and Fig. 2f, 180 °C/6 h). The corresponding particle size frequency his tograms are shown in Fig. 2e′ and f′ respectively.

Fig. 3 shows low magnification TEM images of crystals oriented with the c axis perpendicular to the electron beam with the corre sponding particle size frequency histograms. HHN and LHN sam ples, both heated at 180 °C/4 h and 180 °C/6 h are shown. Well crystallized lamellar crystals are oriented along the $[11\bar{2}0]$ orien tation of the brucite hexagonal structure, as confirms the electron diffraction pattern (Fig. 3d). A non agglomerated lamellar crystal obtained from HHN 180 °C/4 h (Fig. 3a) with a particle size of 307 nm (long length) and a thickness of 40 nm is compared to the typical idealized brucite crystal disposed in the same orienta tion (Fig. 3a, insert). Lamellar crystals obtained with HHN samples at 180 °C/4 h (Fig. 3b b′) and 180 °C/6 h (Fig. 3c c′) and their cor responding particle size frequency histograms (long length size) indicate a poly dispersed distribution. In the lower part of the fig ure, LHN samples heated at 180 °C/4 h (Fig. 3e e′) and 180 °C/6 h (Fig. 3f f′) are shown. In this orientation is possible to measure the thickness, indicating that the samples with short heating times are thinner than those subjected to prolonged heating times (Table 2).

The comparison between samples heated at 180 °C during dif ferent reaction times (4 h, 6 h and 12 h) and from two different hydrazine/nitrate concentrations (Table 2) shows a slight tendency to develop larger particles size when higher hydrazine/nitrate con centration and longer reaction times have been used (Fig. 3b, 180/4 h and 3c, 180 °C/6 h). In general, particles have mean sizes around 200 600 nm. However the largest particles are formed when high dose of hydrazine/nitrate and heating of 180°/12 h are used, reaching a mean size around 1026 nm (LHN) to 1240 nm (HHN). The smallest values (209 nm) correspond to particles growth at shorter heating time and low dose of hydra zine/nitrate (180 °C/4 h) (Table 2). However, when the particle sizes are compared with samples subjected to prolonged heating treatment (180 °C/12 h, Fig. 3f) both if have been synthesized using a low dose of hydrazine/nitrate (672 nm) or with high dose hydra zine/nitrate (986 nm), the particle's size is highly increased, due to the prolonged reaction time. In addition, the standard deviations reveal higher values for samples prepared with less hydrazine/ nitrate content.

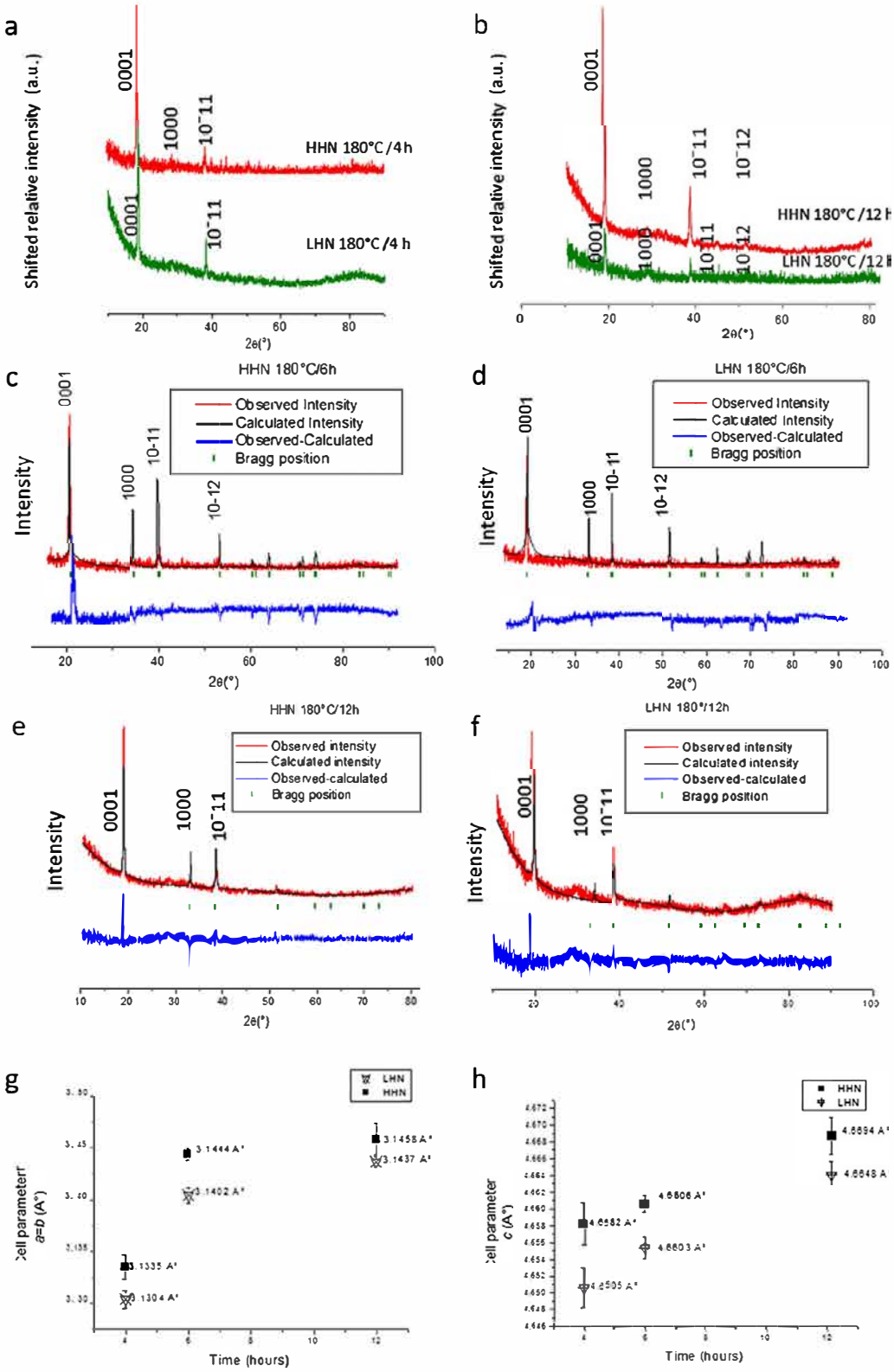

Fig. 1. XRD patterns indexed according to the brucite phase. Comparison among high hydrazine/nitrate (HHN) and low hydrazine nitrate (LHN) samples (180 °C/4 h, (a) and 180 °C/12 h, (b)). Rietveld refinement graphics showing differences in the adjustment depending on the hydrazine/nitrate content: 180 °C/6 h samples (HHN (c), and LHN, (d)) and 180 °C/12 h (HHN (e) and LHN (f)). Calculated cell parameters (in Å), corresponding to $a = b$ (g) and c (h) in the different experimental conditions.

This increase in particle size, highly noticeable after 12 h of heating, reaches values of 111% when the doses of hydrazine/nitrates is high and 180% for the sample prepared with low dose of hydrazine/nitrates, as is observed in particles oriented with the c axis parallel to electron beam (Table 2). In all cases, with the raise of heating time, an increase in particle size occurs, resulting to be far superior to size after 4 h of heating, with values of increase around 230%, in samples with high concentration hydrazine/nitrates and 390% for low hydrazine/nitrate doses (Table 2).

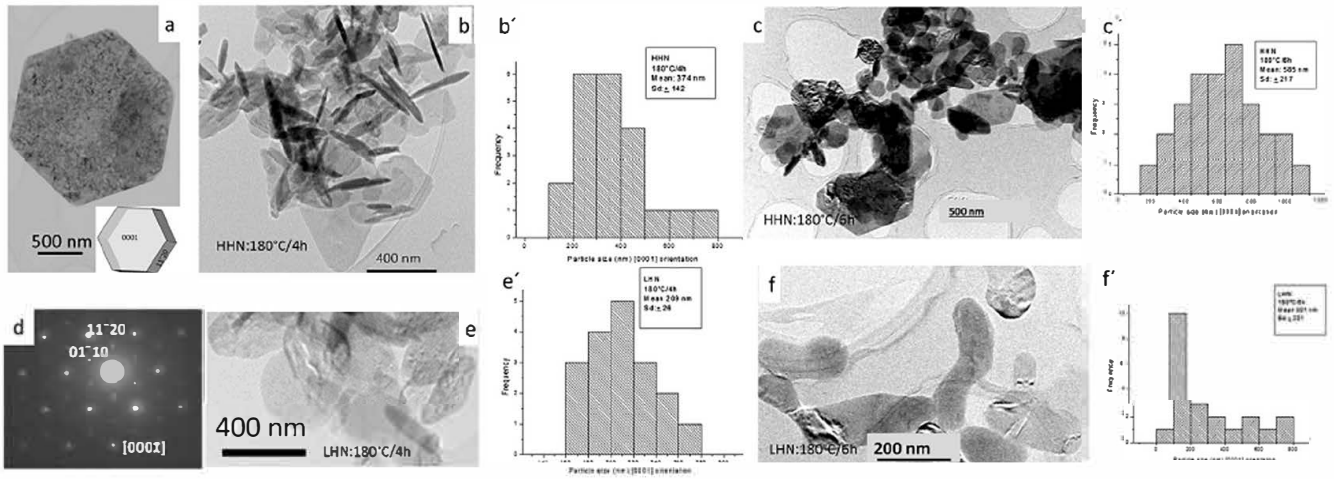

Fig. 2. Low magnification TEM images showing hexagonal and lamellar shapes (the hexagonal platelets are oriented with the *c* axis parallel to the electron beam) in samples prepared with high hydrazine/nitrate (HHN) and low hydrazine/nitrate (LHN). A hexagonal platelet is shown in (a). The typical shape is shown insert. HHN: 180 °C/4 h (b), 180 °C/6 h (d) with the respective particle size frequency histograms (b′ and c′). LHN: 180 °C/4 h (e) and 180 °C/6 h (f) and their respective frequency histograms (e′ and f′). The electron diffraction pattern is oriented along [0001] zone axis of brucite phase (d). Images taken at 200 kV acceleration voltage.

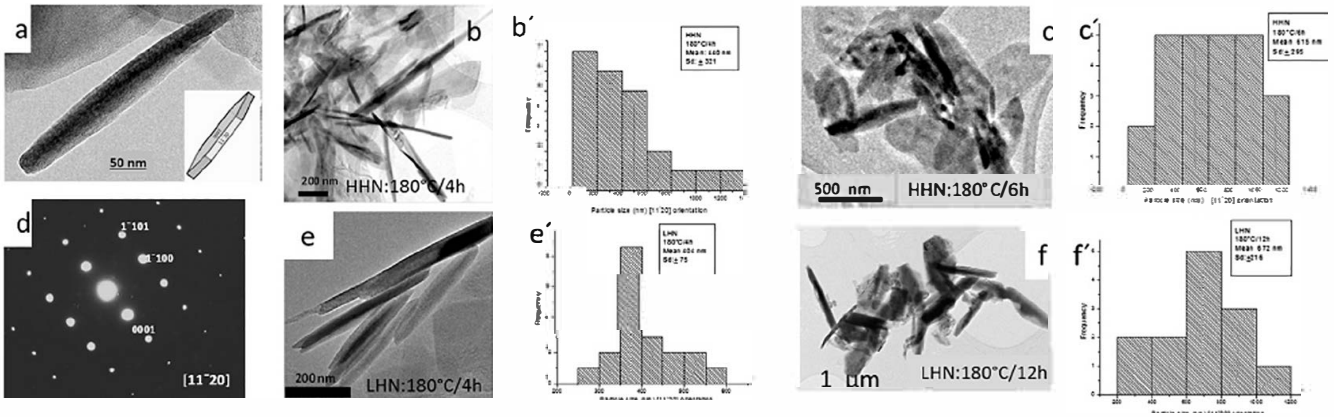

Fig. 3. Low magnification TEM images corresponding to lamellar crystals observed with the beam perpendicular to *c* axis in samples prepared with high hydrazine/nitrate (HHN) and low hydrazine/nitrate (LHN). A lamellar crystal is shown in (a). The typical shape is shown insert. HHN: 180 °C/4 h (b), 180 °C/6 h (c) with the respective particle size frequency histograms (b′ and c′). LHN: 180 °C/4 h (e) and 180 °C/12 h (f) and their respective frequency histograms (e′ and f′). The electron diffraction pattern is oriented along [1 0 $\bar{1}$ 2] zone axis of brucite phase (d). Images were taken at 200 kV acceleration voltage.

Table 2
Statistical values obtained for particle size in samples prepared with low and high concentration of hydrazine/nitrate at different times of reaction (*increment value respect to samples prepared at 4 h).

Temperature and time of reaction	HHN	Particle size increase (%)	LHN	Particle size increase (%)	Orientation
180 °C/4 h	Mean 374 nm Sd: ±142	–	Mean 209 nm Sd: ±26	–	Beam parallel to *c* axis Long length
	Mean: 440 nm Sd: ±321	–	Mean: 404 nm Sd: ±75	–	Beam perpendicular to *c* axis Long length
	Mean: 44 nm Sd: ±17	–	Mean: 43 nm Sd: ±12.5	–	Thickness Short length
180 °C/6 h	Mean: 585 nm Sd: ±217	56.42	Mean 365 nm Sd: ±140	74.64	Beam parallel to *c* axis Long length
	Mean: 615 nm Sd: ±295	39.77	Mean: 584 nm Sd: ±46	44.55	Beam perpendicular to *c* axis Long length
	Mean: 88 nm SD: ±37	100	Mean: 78 nm Sd: ±6	81.40	Thickness Short length
180 °C/12 h	Mean: 1240 Sd: ±430	111.97 (231.55*)	Mean: 1026 Sd: ±555	181.10 (390.91*)	Beam parallel to *c* axis Long length
	Mean: 986 nm Sd: ±372	60.33 (124.09*)	Mean: 672nm Sd: ±216	15.07 (66.34*)	Beam perpendicular to *c* axis Long length
	Mean: 156 nm Sd: ±45	77.27 (254.55*)	Mean: 133 nm Sd: ±87	70.51 (209.30*)	Thickness Short length

With respect to the particle thickness, its values are below 100 nm in treatments at 4 and 6 h, both in high concentration as in low concentration samples. In the shorter time of heating (4 h), particles maintain similar thicknesses (42 44 nm, for HHN and LHN respectively). After 6 h of heating the thickness is increased 100% in the HHN sample (88 nm), resulting slightly lower (81%) in the LHN sample (78 nm). However, when it has reached a heating time of 12 h, its thickness has grown above 100 nm, so that the particles reach thickness between 156 nm for HHN and 133 nm for LHN samples, producing an increase of 77% in high dose hydrazine/nitrate sample and of 70% in the low con centration sample respect to the samples heated during 6 h.

From these observations can be deduced how the concentration of hydrazine/nitrate and the reaction time play an important role in controlling particle size. Thus, nanostructured or micrometric particles can be developed, mainly by controlling the times of reac tion. Furthermore, better crystallized particles can be obtained with highest dose of hydrazine/nitrate.

3.3. Textural and structural behavior: effect of experimental conditions

Textural differences have been observed through the low and high resolution TEM. In Fig. 4, the comparison among samples obtained by using high dose (Fig. 4a, 180°/4 h and Fig. 4c, 180 °C/6 h) with samples prepared with low concentration (Fig. 4b, 180°/4 h and Fig. 4d, 180 °C/6 h) of hydrazine/nitrate indi cates differences in the developing of structural defects including strains and dislocations, as observed in the low magnification TEM images. While the samples prepared with higher dose of hydrazine/nitrate develop strong preferential orientations (Fig. 4a and d), the samples prepared with low dose have defects with aleatory distribution. On the other hand, the density of defects is lower in samples prepared with low doses of hydra zine/nitrate. This observation could be an important clue in the dif ference respect to the kinetic of reaction, during the dehydration process.

3.4. Evaluation of the dehydration process of $Mg(OH)_2$ caused by electron irradiation during the TEM analysis: effect of experimental conditions

The dehydration of brucite and the crystal structural evolution from $Mg(OH)_2$ to MgO is controlled trough the morphological and structural changes during the exposition to electron beam.

Fig. 5 shows the results of the exposition of two samples of bru cite, obtained at high (180 °C/4 h, Fig. 5a c) and low concentration (180 °C/12 h, Fig. 5d f) of hydrazine/nitrate using an accelerator voltage of 300 kV. The calculated porosity images are shown in Fig. 5c and f. In both cases dark areas correspond to porous sur faces. In the first case (Fig. 5a c), the lamella oriented along the $[10\bar{1}0]$ direction undergoes a change in the pore structure with the development of a highly porous surface since the earlier stage of irradiation. Changes in porosity are clearly visible, which obey to the release of water from the structure. The outer region indicates porosities about 40 49%, while the inner region varies between ~26 and 28%, reaching up 19% in the innermost region where the hydroxide is still present.

In the second case (Fig. 5d f), the lamella corresponding to the sample obtained with low hydrazine content at 180 °C/12 h has reached a lower porosity (27 32%) although with similar values (47%) in the outermost region. By contrast, the innermost region has not been affected by the irradiation, where the porosity value is scarcely of 0.9%. This behavior is common in different hydroxides [38 40], in which the dehydration process usually begins at the

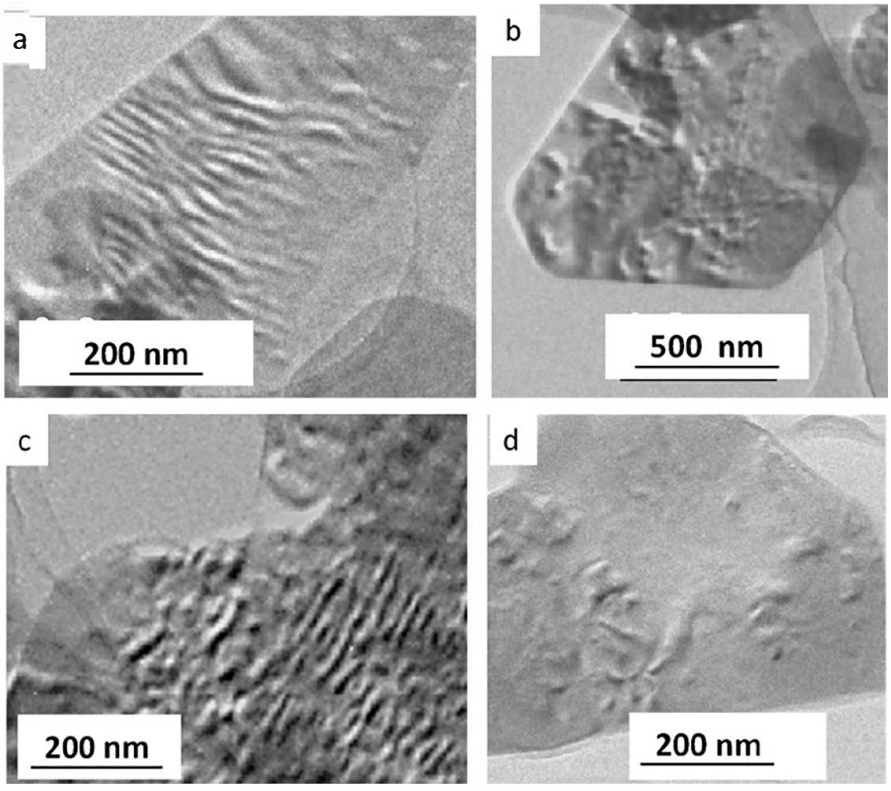

Fig. 4. Low magnification TEM images showing strains formed in samples obtained by high concentration of hydrazine/nitrate (a), 180°/4 h and c, 180 °C/6 h) and low concentration of hydrazine/nitrate ((b), 180°/4 h and d 180 °C/6 h). A strong preferential orientation is observed in samples prepared with HHN content. Images were taken at 200 kV acceleration voltage.

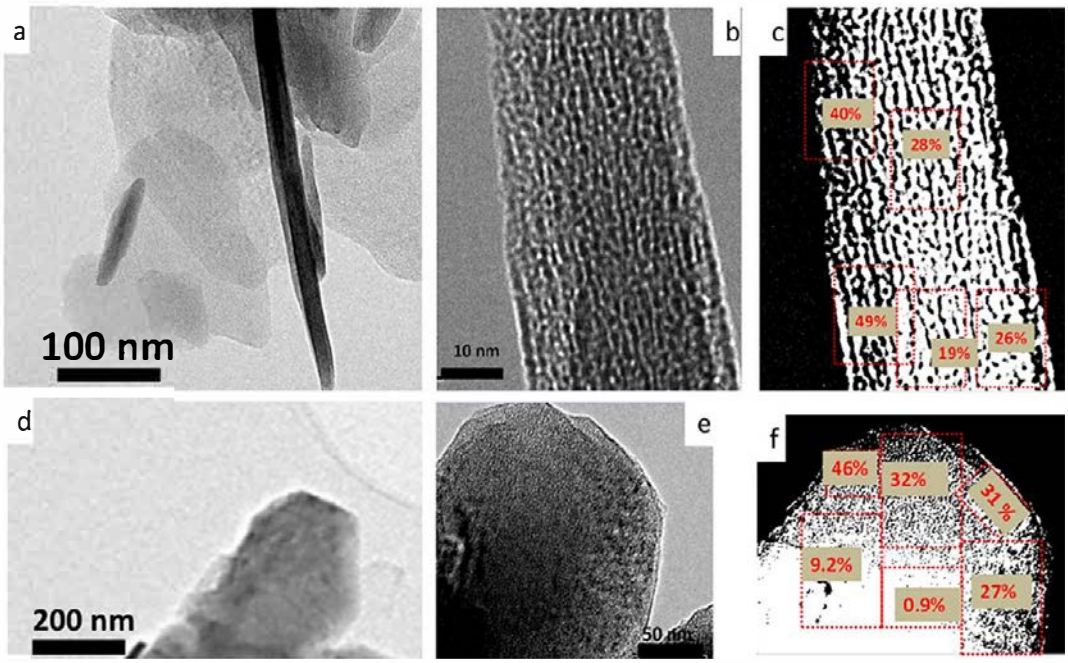

Fig. 5. Changes in porosity during the exposition to electron beam. Comparison among a sample prepared with high concentration of hydrazine/nitrate (180 °C/12 h, (a–c)) and a sample prepared with low hydrazine/nitrate concentration (180 °C/12 h, (d–f)). Calculated porosity images are shown in c and f. The images were captured with 300 kV acceleration voltage.

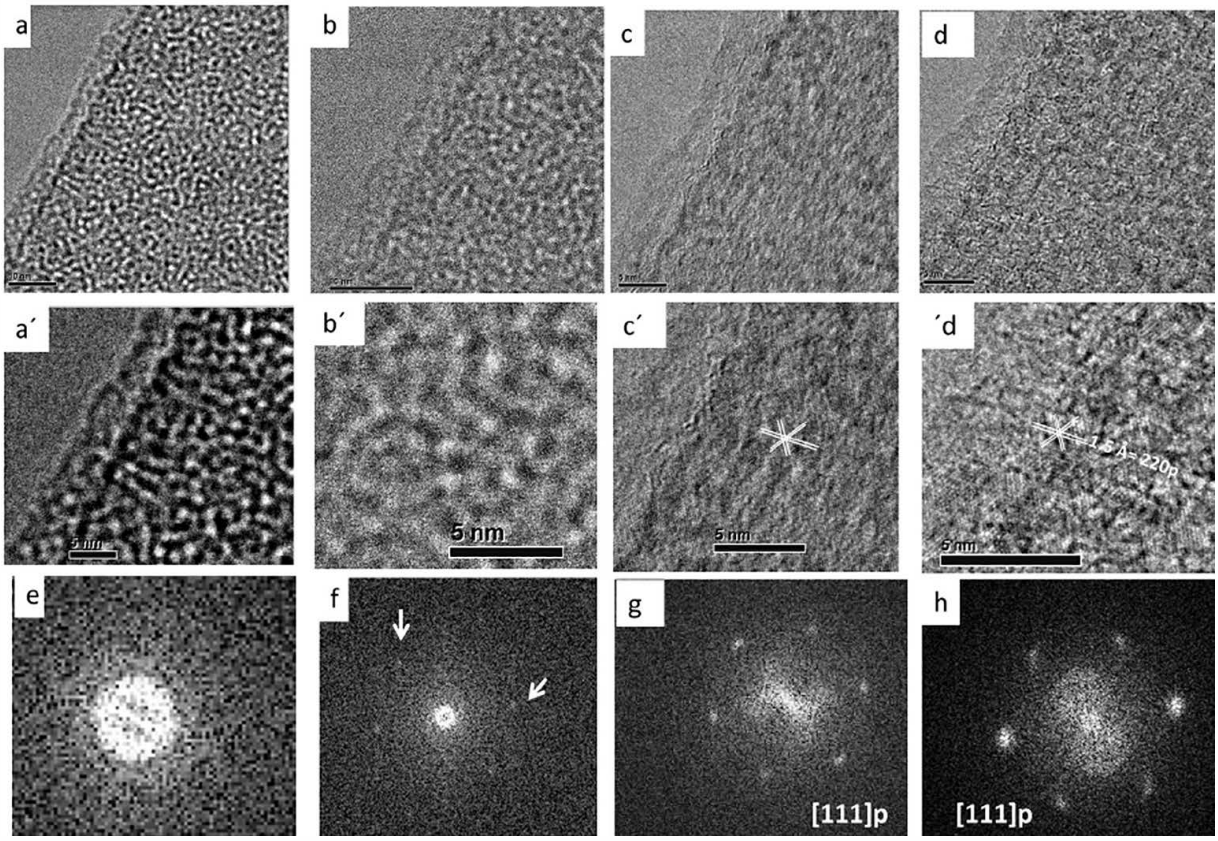

Fig. 6. TEM images showing the dehydration process in a sample obtained with high hydrazine/nitrate dose (180 °C/6 h). The advance of the dehydration is shown from left to right (a to d). The initial stage (a and a′) intermediate stages (b and b′, and c and c′) and the final stage (d, and d′). Figures a′, b′, c′ and d′ correspond to enlargements of each step. The corresponding FFTs along the process are shown in figures e, f, g, h respectively. The elapsed time was 20 s from the start time of observation. The sequence of images was captured with 300 kV acceleration voltage.

edge of the specimen and progresses towards the center. The development of a highly porous surface observed in the sample with high content of hydrazine/nitrate from the very early stage of dehydration is clearly caused by the excess of reagents, unlike less concentrated dose, where the increase in porosity as a result of the output of hydroxyl ions turns out to be slower.

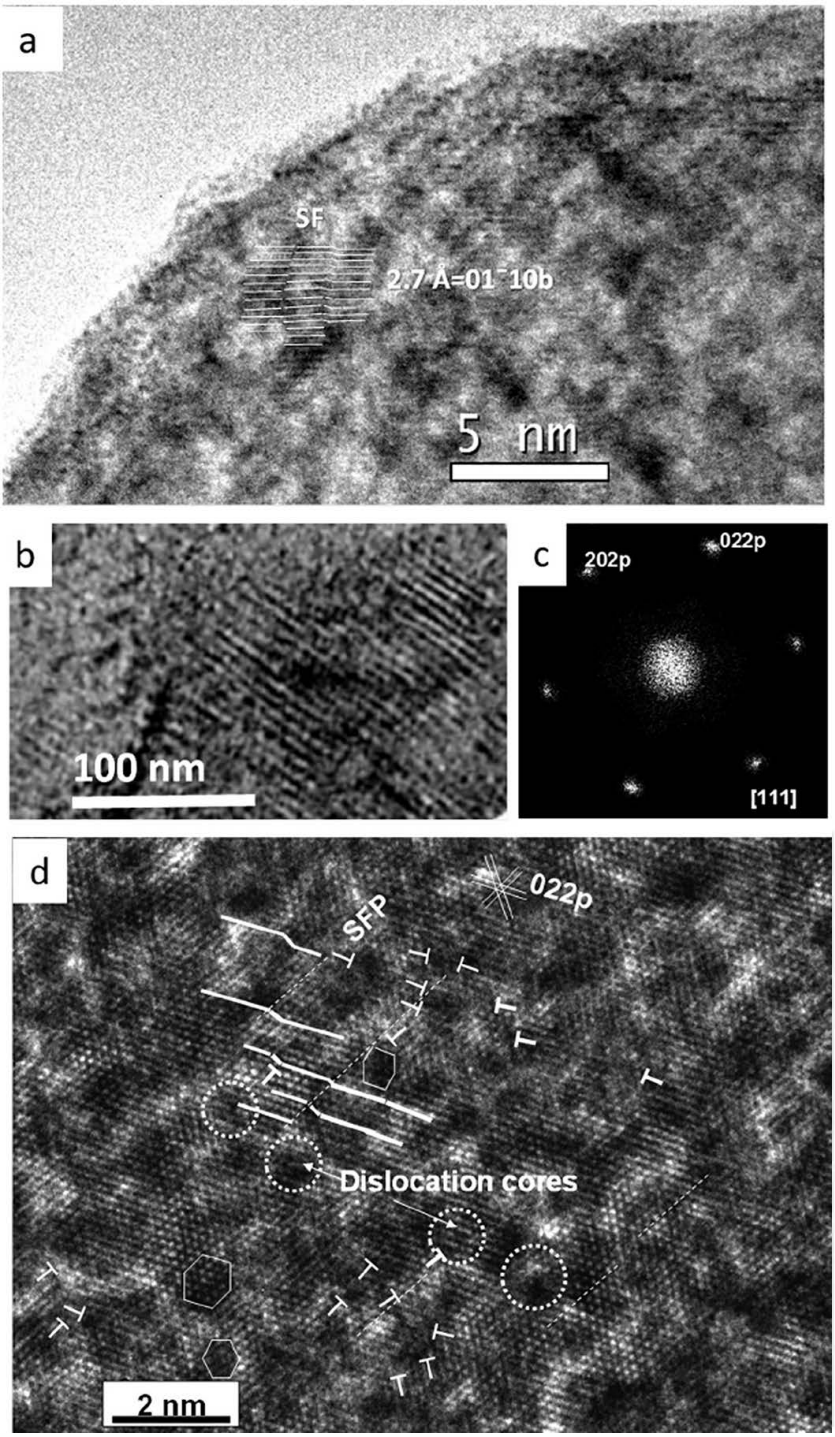

Fig. 7. HRTEM image of the sample synthesized with high concentration of hydrazine/nitrate at 180 °C/6 h. (a) was taken at 200 kV acceleration voltage showing the external region, some atomic planes of brucite are observed. Low magnification high resolution TEM showing moiré fringes (b). HRTEM image captured at 300 kV acceleration voltage showing atomic defects, stacking faults (SF), extra atoms and dislocations. The corresponding FFT oriented along $[1\,1\,1]_{(periclase)}$ is shown in figure c.

The dehydration process in a sample obtained with high hydra zine/nitrate dose (180 °C/6 h) observed with 300 kV of acceleration voltage is shown in Fig. 6. Brucite starts to develop a highly amor phous rim which coincides with the growth of the porous surface (Fig. 6a, a′, b and b′), which is transformed to a high disordered per iclase after 20 s of exposure to the electron beam. As deduced from the FFTs (Fig. 6e h), in the first stage, the amorphous character is confirmed, followed for the development of planes with (1.5 Å) *hkl* distance and crystallographic arrangement corresponding to the {2 2 0} periclase, to finally form the typical periclase structure along the [1 1 1] orientation (Fig. 6h).

The sample synthesized with high concentration of hydrazine/ nitrate at 180 °C/6 h (Fig. 7) shows the development of a rim around the particle, where atomic planes are still visible, during the exposition to 200 kV. In the early stage of irradiation, the bru cite is still present, as deduced from the periodicity of 2.7 Å equiv alent to the $\{01\bar{1}0\}$ plane of the brucite phase (Fig. 7a). Besides a high density of moiré fringes in the low magnification high resolu

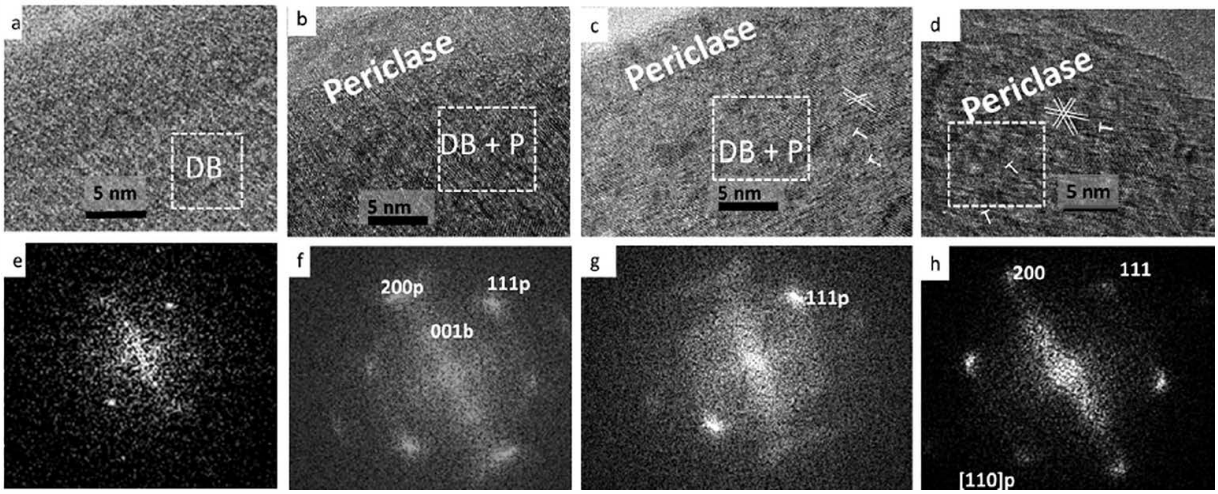

Fig. 8. TEM images showing the dehydration process in a sample obtained with low hydrazine/nitrate dose (180 °C/12 h). The advance of the dehydration is shown from left to right (a to d). The initial stage (a) intermediate stages (b and c) with simultaneous presence of dehydrated brucite (DB) and periclase (P); and the final stage with periclase oriented along [1 1 0] direction (d). The corresponding FFTs along the process are shown in figures e, f, g, h respectively. The elapsed time was 120 s from the start time of observation. The sequence of images was captured using 300 kV acceleration voltage.

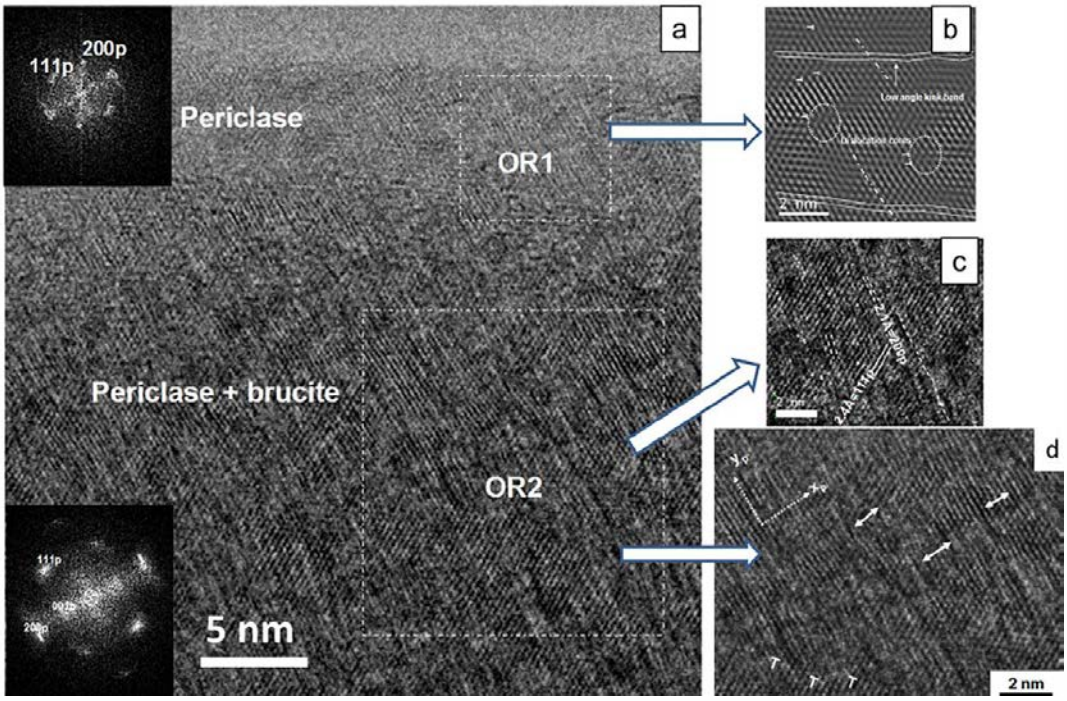

Fig. 9. HRTEM image of the sample synthesized with low concentration of hydrazine at 180 °C/12 h. Two orientation relationship (OR) are demarked. The external region (OR1) corresponds to periclase while the internal includes brucite and periclase. Details of atomic defects are shown in the enlarged images (b, c and d). The corresponding FFTs are shown as insert. For details see the text.

tion image (Fig. 7b) is observed. These observations correspond to the sample shown in Fig. 4c, where highly oriented defects are pre sent in the brucite crystal oriented along the [0001] direction. The HRTEM image taken with higher acceleration voltage (300 kV) shows a series of stacking faults (SF) and dislocation cores in the periclase planes with {022} periodicity (Fig. 7d). A number of edge dislocations are also identified. Local vacancy defects generated by missing atoms are likewise observed. These extra atoms induce extrinsic stacking faults (SF), favoring dislocation movements. The Fourier transform confirms the presence of typical periclase, with well defined, high intensity spots for {220} planes along [111] orientation (Fig. 7c).

Similarly, the dehydration process was controlled in a particle prepared with low hydrazine content and a heating of 180°/12 h using 300 kV (Fig. 8). The brucite oriented along the [11$\bar{2}$0] is con verted to periclase by topotactic transformation, in a process that took around 120 s. The different steps are clearly visible. In the early stage of dehydration, the identification of a rim with different orientation relationship (Fig. 8a), and atomic planes corresponding to a partially dehydrated brucite (confirmed by FFT, Fig. 8e), grad ually evolves until to be able to identify the two phases, the hydrated inside and the dehydrated on the edge (Fig. 8b and c). However, the coexistence of brucite and periclase is common due to differences in the dehydration rate. In the final step, previous

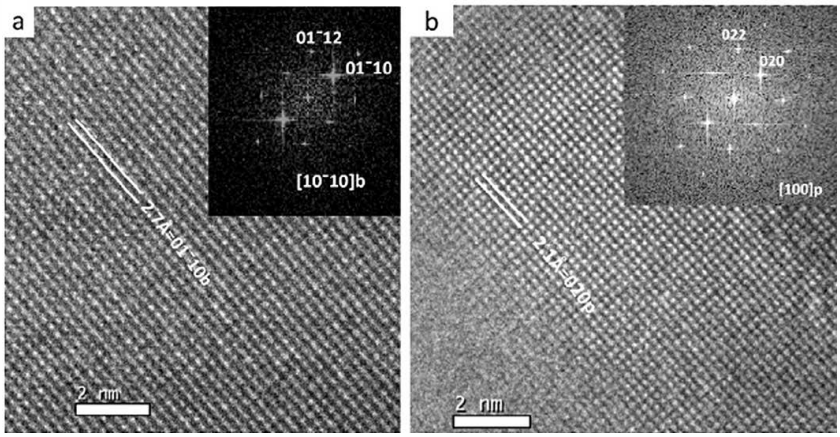

Fig. 10. Dehydration process along the [10$\bar{1}$0] orientation of the brucite phase. Sample prepared with low concentration of hydrazine/nitrate and heated at 180 °C/6 h. The initial stage (a) shows the brucite phase and its transformation to periclase after 120 s of irradiation (b). The corresponding FFTs are shown as insert. Images captured at 300 kV acceleration voltage.

to the amorphisation, the periclase is clearly formed (Fig. 8d). The FFTs confirm the simultaneous presence of brucite and periclase (Fig. 8f), the development of high disordered periclase showing the reflections of the {111} planes (Fig. 8f and g), until finally after 120 s the periclase along [110] is formed (Fig. 8h).

An enlargement of one step of this process is observed in the HRTEM of Fig. 9. The sample synthesized at 180 °C/12 h, exhibits two regions with different orientation relationship (OR). The very thin (scantly 5 nm thick) outer region (OR1) is converted com pletely to periclase, as confirmed by FFT (upper left insert). In con trast, the inner region (OR2) exhibits periodicity with atomic planes denoting the presence of both brucite and periclase. The respective FFT (lower left insert) confirms that in addition to peri clase planes {111} and {200}, {0001} brucite planes were still present. OR1 (Fig. 9b) exhibits a calculated IFFT image where low angle kinks generally gives rise to fault planes parallel to {200}. In OR2, periclase brucite intergrowth is visible, with defects run ning parallel to {200} periclase (arrows).

The dehydration process along the [10$\bar{1}$0] orientation is slightly different of the observed along the [0001] and [11$\bar{2}$0] ori entations. As shown in Fig. 10, a very high ordered and crystalline character is evident. In this case the sample has been prepared with low concentration of hydrazine/nitrate and heated at 180 °C/6 h. In an early step of irradiation, the distances between lattice fringes adjust to the brucite structure oriented according to the [10$\bar{1}$0] zone axis of the brucite phase. After 120 s of irradi ation, the brucite is transformed to periclase as confirm the FFTs for brucite (Fig. 10, inset) and periclase (Fig. 10b, inset) phases. Besides the HRTEM images show atomic planes for {01$\bar{1}$0} for bru cite (Fig. 10a) and {020} for periclase (Fig. 10b).

These observations confirm how MgO tends to grow with sur face termination by {200} and their family planes to acquire the most stable atomic arrangement [41,42]. In the present case, along the periclase basal plane less atomic defects and dislocations are developed, unlike octahedral surfaces, where a high density of defects accelerates the dehydration. This transformation is faster when the octahedral surfaces are irradiated in comparison with the basal surfaces of periclase.

In relation to the dehydration process, several reports have studied the chemistry of the dehydroxylation [14,15,39]. According to Green [43], the presence of water molecules in the system impacts the reaction kinetics heavily, both in terms of nucleation and end product, MgO. Water appears to improve nucleation by governing the size of the MgO crystals formed. Both cationic and anionic vacancy defects are generated in the process. The differ ences in vacancy defect concentrations favor material migration, including O^2 ion displacement due to oxygen desorption to form water at a site adjacent to the site where it was initially adsorbed, then adsorption/desorption gives rise to rapid crystal growth and agglomeration with the concomitant reduction in MgO surface area [44].

3.5. Effect of experimental conditions on the morphology, shape and particle size

Undoubtedly, the hydrazine/nitrate concentration has had a fundamental role in the morphological variations as well as on the crystal growth of the different nanoparticles, and its response to dehydration process by the electron beam.

Independently of reaction time, the particles prepared with low concentration of hydrazine/nitrate tend to develop amorphous edges, which are visible in particles oriented along the [0001].

The tendency to develop lamellas of longer length is favored when the particles have been prepared from a higher hydrazine/ nitrate concentration. In general, the particles present a mean size around 200 600 nm, although eventually may have sizes above 1 μm. The lowest values correspond to particles grown at shorter reaction time and low dose of hydrazine/nitrate (180 °C/4 h). The standard deviation calculations reveal higher values for samples prepared with less hydrazine/nitrate content. The reaction times and changes in porosity, as a result of the output of hydroxyl ions, during the exposition to high energy are different when samples have been prepared with high or low doses of reagents. The fast development of a highly porous surface is observed in the sample with high content of hydrazine/nitrate from the very early stage of dehydration (the total time of transformation was 20 s). However, when samples are prepared with low content of reagents, the porosity changes turn out to be slower (in the example presented, the time elapsed from the beginning of exposure was 120 s). How ever, it is important to clarify that the total time of dehydration may vary depending on the sample thickness or the density and orientation of structural defects.

The presence of highly oriented strains has been observed in samples prepared with high hydrazine/nitrate content. Although the presence of these strains has been observed also in samples prepared with low concentration of hydrazine/nitrate its density is lower and is randomly disposed along the surface. This arrange ment and density in samples with more content of hydrazine/ nitrate could be important, since it would contribute to a rapid transformation of the hydroxide, the presence of an amorphised

cortex, the generation of a quick porous surface, or the rapid nucle ation of the periclase phase. As described in similar experiments [45], hydrated hydrazine serves as a mineralization template in the hydrothermal process which induces the specifically orienta tion of the crystallization.

In other synthesis procedures, a decrease in crystallinity has been observed when samples have been prepared with very high doses of hydrazine [29]. The development of plate like morpholo gies with low doses or the presence of morphologies slightly dis torted depends seriously on the concentration applied [46,47] or the way as hydrazine be applied [30].

4. Conclusion

Micro and nanostructured $Mg(OH)_2$ (brucite) particles obtained by hydrothermal method exhibit different characteristics accord ing to the hydrazine/nitrate content used during the synthesis reaction by hydrothermal method. Although the samples have sim ilar particle size (200 600 nm), the tendency to form bigger crys tals is observed in samples prepared with high hydrazine (0.14 M) and nitrate (0.24 g) content. On the other hand, the pres ence of preferential orientations observed in samples with high hydrazine/nitrate content, increases the reaction kinetic. During the electron beam irradiation, the rapid formation of a porous sur face, the amorphised cortex or the presence of higher content of defects in samples prepared with high content of hydrazine/ nitrate, undoubtedly affect the crystal growth, the particle size dis tribution, the morphology and therefore the dehydration process. Conversely, the presence of crystals slightly smaller with rounded borders in samples prepared with low hydrazine (0.0002 M) and nitrate (0.12 g) content and randomly scattered defect surfaces contribute to establish significant differences in the kinetic of reac tion in both types of routines.

The Rietveld refinements show how unit cell parameters of samples prepared with high hydrazine/nitrate content are bigger in comparison with those obtained with samples prepared with low hydrazine/nitrate content. Besides, smaller unit cell parame ters are typical of samples with low reaction time (180 °C/4 h).

This research provides important information to control the crystal growth and the particles morphology. In order to determine the appropriate particle size with the desired morphology, and a narrow particle size distribution, it is necessary to test different concentrations of hydrazine and nitrate during preparation of the samples. Depending on the field of application, the use of nanopar ticles prepared by hydrothermal method including hydrazine and nitrate, in fields as diverse as catalysis, consolidating agent or for flame retardant applications, for instance, a careful monitoring is advisable for obtaining the most suitable results.

Acknowledgments

This present research was funded by the Community of Madrid under the GEOMATERIALES II project (S2013/MIT 2914), by the Complutense University of Madrid's Research Group: "The alter ation and conservation of stone heritage" (921349), the Autono mous Region Program of Madrid, MULTIMAT CHALLENGE (ref. S2013/MIT 2862), the Innovation and Education Ministry ref. (MAT2013 47460 C5 5 P), the Mat201019837/C06 05 and the Ministry of Education, Science and Technological Development of Serbia (OI 1612046) projects. The authors are indebted to the Petrophysical Laboratory IGEO, affiliated with the Moncloa Cam pus of International Excellence CEI 09 009(UCM UPM), the Her itage Laboratory Network in Science and Technology for Heritage Conservation (RedLabPat,) and the Materials Science Department (Carlos III University of Madrid). Thanks go also for the assistance provided by Adrian Gómez Herrero and Juan Luis Baldonedo of the National Microscope Centre (Madrid, Spain).

References

[1] Ch. Schacht, Refractories Handbook, Marcel Dekker Inc. CRC Press, USA, 2004, ISBN 08247.5654-1.
[2] J. Formosa, J.M. Chimenos, A.M. Lacasta, L. Haurie, Thermal study of low-grade magnesium hydroxide used as fire retardant and in passive fire protection, Thermochim. Acta 515 (2011) 43–500.
[3] Y. Zhang, T. He, W. Cao, Y. Cheng, X. Zhang, Study on application of brucite fiber to composite paint with energy-saving and thermal insulation, New Build. Mater. 8 (2007) 026.
[4] H.U. Rammelberg, J.K. Köllner, T. Schmidt, O. Opel, W. Ruck, Hydration and dehydration of salt hydrates and hydroxides for thermal energy storage kinetics, energy release and cyclability, Appl. Energy 154 (2015), http://dx.doi.org/10.1016/j.apenergy.2015.02.011.
[5] M. Zamengo, J. Ryu, Y. Kato, Chemical heat storage of thermal energy from a nuclear reactor by using a magnesium hydroxide/expanded graphite composite material, Energy Proc. 71 (2015) 293–305.
[6] M.A. Shand, The Chemistry and Technology of Magnesia, John Wiley & Sons, Inc., New Jersey, 2006.
[7] Y. Zhang, M. Ma, X. Zhang, B Wang, R. Liu, Synthesis, characterization, and catalytic property of nanosized MgO flakes with different shapes, J. Alloy. Compd. 590 (2014) 373–379.
[8] B.S. Necula, L.E. Fratila-Apachitei, A. Berkani, I. Apachitei, J. Duszczyk, Enrichment of anodic MgO layers with Ag nanoparticles for biomedical applications, J. Mater. Sci. – Mater. Med. 20 (2009) 339–345.
[9] K. He, Y.M. Dong, Z. Li, L. Yin, A.M. Zhang, Y.C. Zheng, Catalytic ozonation of phenol in water with natural brucite and magnesia, J. Hazard. Mater. 159 (2) (2008) 587–592.
[10] I. Dumitriu, R.C. Fierascu, R.M. Ion, R.I. Bunghez, M.C. Corobea, Nanotechnology applied in archaeometry: restoration and conservation, Adv Top Optoelectron, Microelectron, Nanotechnol Int Soc Opt Photon, Int Soc Opt Photon (2010) [p. 78211I-78211I].
[11] P. Baglioni, D. Chelazzi, Nanoscience for the Conservation of Works of Art, Nanoscience & Nanotechnology 28, The Royal Society of Chemistry, 2013.
[12] R. Giorgi, C. Bozzi, L.G. Dei, C. Gabbiani, B.W. Ninham, P. Baglioni, Nanoparticles of $Mg(OH)_2$: synthesis and application to paper conservation, Langmuir 21 (2005) 8495–8501.
[13] M. Müller, Symmetry Relationships Between Crystal Structures: Applications of Crystallographic Group Theory in Crystal Chemistry, Oxford University Press, Oxford, 2013.
[14] M.C. Ball, H.F.W. Taylor, The dehydration of brucite, Mineral. Mag. 32 (253) (1961) 754–766.
[15] M.G. Kim, U. Dahmen, A.W. Searcy, Structural transformations in the decomposition of $Mg(OH)_2$ and $MgCO_3$, J. Am. Ceram. Soc. 70 (1987) 146–154.
[16] M.J. McKelvy, R. Sharma, A.V. Chizmeshya, R.W. Carpenter, K. Streib, Magnesium hydroxide dehydroxylation: in situ nanoscale observations of lamellar nucleation and growth, Chem. Mater. 13 (3) (2001) 921–926.
[17] M.A. Asoro, P.J. Ferreira, D. Kovar, In situ transmission electron microscopy and scanning transmission electron microscopy studies of sintering of Ag and Pt nanoparticles, Acta Mater. 81 (2014) 173–183.
[18] N. Thangaraj, K.H. Westmacott, U. Dahmen, HVEM studies of the sintering of MgO nanocrystals prepared by $Mg(OH)_2$ decomposition, Ultramicroscopy 37 (1) (1991) 362–374.
[19] A.R. Bueno, R.F.M. Oman, P.M. Jardim, N.A. Rey, R.R. de Ayillez, Kinetics of nanocrystalline MgO growth by the sol–gel combustion method, Micropor. Mesopor. Mater. 185 (2014) 86–91.
[20] G. Taglieri, B. Felice, V. Daniele, F. Ferrante, $Mg(OH)_2$ nanoparticles produced at room temperature by an innovative, facile, and scalable synthesis route, J. Nanopart. Res. 17 (10) (2015) 1–13.
[21] A. Pilarska, M. Wysokowski, E. Markiewicz, T. Jesionowski, Synthesis of magnesium hydroxide and its calcinates by a precipitation method with the use of magnesium sulfate and poly(ethylene glycols), Powder Technol. 235 (2013) 148–157.
[22] F. Meshkani, M. Rezaei, Facile synthesis of nanocrystalline magnesium oxide with high surface area, Powder Technol. 196 (2009) 85–88.
[23] Z. Ling, M. Zheng, Q. Du, Y. Wang, J. Song, W Dai, Synthesis of mesoporous MgO nanoplate by an easy solvothermal–annealing method, Solid State Sci. 12 (13) (2011) 2073–2079 [12, 13].
[24] S. Kar, S. Chaudhuri, Synthesis and characterization of one-dimensional MgO nanostructures, J. Nanosci. Nanotechnol. 6 (2006) 1447–1452.
[25] Q. Wang, C. Li, M. Guo, L. Sun, C. Hu, Hydrothermal synthesis of hexagonal magnesium hydroxide nanoflakes, Mater. Res. Bull. 51 (2014) 35–39.
[26] M.S. Bakshi, How surfactants control crystal growth of nanomaterials, Cryst. Growth Des. 16 (2) (2015) 1104–1133.
[27] N. Wald, J. Boreham, R. Doll, J. Bonsall, Occupational exposure to hydrazine and subsequent risk of cancer, Br. J. Ind. Med. 41 (1) (1984) 31–34.
[28] E. Sotaniemi, J. Hirvonen, H. Isomäki, J. Takkunen, J. Kaila, Hydrazine toxicity in the human. Report of a fatal case, Ann. Clin. Res. 3 (1) (1971) 30–33.
[29] K.C. Preetha, T.L. Remadevi, Effect of hydrazine hydrate concentration on structural, surface 2016morphological and optoelectronic properties of SILAR deposited PbSe thin films, Mater. Sci. Semicond. Process. 39 (2015) 178–187.

[30] D. Maiti, U. Manju, S. Velaga, P.S. Devi, Phase evolution and growth of iron oxide nanoparticles: effect of hydrazine addition during sonication, Cryst. Growth Des. 13 (8) (2013) 3637–3644.
[31] D. Polsongkram, P. Chamninok, S. Pukird, L. Chow, O. Lupan, G. Chai, H. Khallaf, S. Park, A. Schulte, Effect of synthesis conditions on the growth of ZnO nanorods via hydrothermal method, Physica B 403 (19) (2008) 3713–3717.
[32] K.C. Pingali, S. Deng, D.A. Rockstraw, Effect of ammonium nitrate in the average size reduction of nanoparticles of silver, nickel and ruthenium synthesized from flash pyrolysis, in: AIChE Annual Meeting, Conference Proceedings, 2005, pp. 14129–14146.
[33] K. Byrappa, T. Adschiri, Hydrothermal technology for nanotechnology, Prog. Cryst. Growth Charact. Mater. 53 (2) (2007) 117–166.
[34] A. Sierra-Fernandez, L.S. Gómez-Villalba, L. Muñoz, G. Flores, R. Fort González, M.E. Rabanal Jiménez, Effect of temperature and reaction time on the synthesis of nanocrystalline brucite, Int. J. Mod. Manuf. Technol. 6 (1) (2014) 50–54.
[35] J. Rodriguez-Carvajal, FULLPROF: a program for Rietveld refinement and pattern matching analysis, Satellite Meeting on Powder Diffraction of The XV Congress of the IUCr, Toulouse, France, vol. 127, 1990.
[36] J.W. Edington, Interpretation of Transmission Electron Micrographs, Macmillan Education, UK, 1975.
[37] T. Nagai, T. Hattori, T. Yamanaka, Compression mechanism of brucite: an investigation by structural refinement under pressure, Am. Mineral. 85 (2000) 760–764.
[38] G. Miehe, S. Lauterbach, H.J. Kleebe, A. Gurlo, Indium hydroxide to oxide decomposition observed in one nanocrystal during in situ transmission electron microscopy studies, J. Solid State Chem. 198 (2013) 364–370.
[39] C.J. Goss, The kinetics and reaction mechanism of the goethite to hematite transformation, Mineral. Mag. 51 (1987) 437–451.
[40] P.A. Van Aken, F. Langenhorst, Nanocrystalline porous periclase aggregates as product of brucite dehydration, Eur. J. Mineral. 13 (2001) 329–341.
[41] X.S. Fang, C.H. Ye, L.D. Zhang, J.X. Zhang, J.W. Zhao, P. Yan, Direct observation of the growth process of MgO nanoflowers by a simple chemical route, Small 1 (4) (2005) 422–428.
[42] J.H. Son, H.K. Yu, J.L. Lee, MgO nano-pyramids structure for enhancement of light extraction efficiency in vertical light-emitting diodes, Opt. Exp. 18 (103) (2010) A403–A410.
[43] J. Green, Calcination of precipitated $Mg(OH)_2$ to active MgO in the production of refractory and chemical grade MgO, J. Mater. Sci. 18 (3) (1983) 637–651.
[44] P.J. Anderson, P.L. Morgan, Effects of water vapour on sintering of MgO, Trans. Faraday Soc. 60 (1964) 930–937.
[45] D. Jin, X. Gu, X. Yu, G. Ding, H. Zhu, K. Yao, Hydrothermal synthesis and characterization of hexagonal $Mg(OH)_2$ nano-flake as a flame retardant, Mater. Chem. Phys. 112 (3) (2008) 962–965.
[46] G. Kaur, M.S. Bakshi, Non ideal mixing of Se–Te in aqueous micellar phase for nanoalloys over the whole mole mixing range with morphology control from nanoparticles to nanoribbons, J. Phys. Chem. C 114 (1) (2009) 143–154.
[47] J.W. Park, E.H. Chae, S.H. Kim, J.H. Lee, J.W. Kim, S.M. Yoon, J.Y. Choi, Preparation of fine Ni powders from nickel hydrazine complex, Mater. Chem. Phys. 97 (2) (2006) 371–378.